Supporting Information

for

AFM Nanoindentation to Quantify the Mechanical Properties of Nano- and Micron-Sized Crystals of a Metal-Organic Framework Material

Zhixin Zeng and Jin-Chong Tan*

Multifunctional Materials & Composites (MMC) Laboratory,
Department of Engineering Science, University of Oxford,
Parks Road, Oxford OX1 3PJ, United Kingdom

**Email of corresponding author:* jin-chong.tan@eng.ox.ac.uk

Table of Contents

1. Characterization of the size of sub-micron ZIF-8 crystals from AFM images

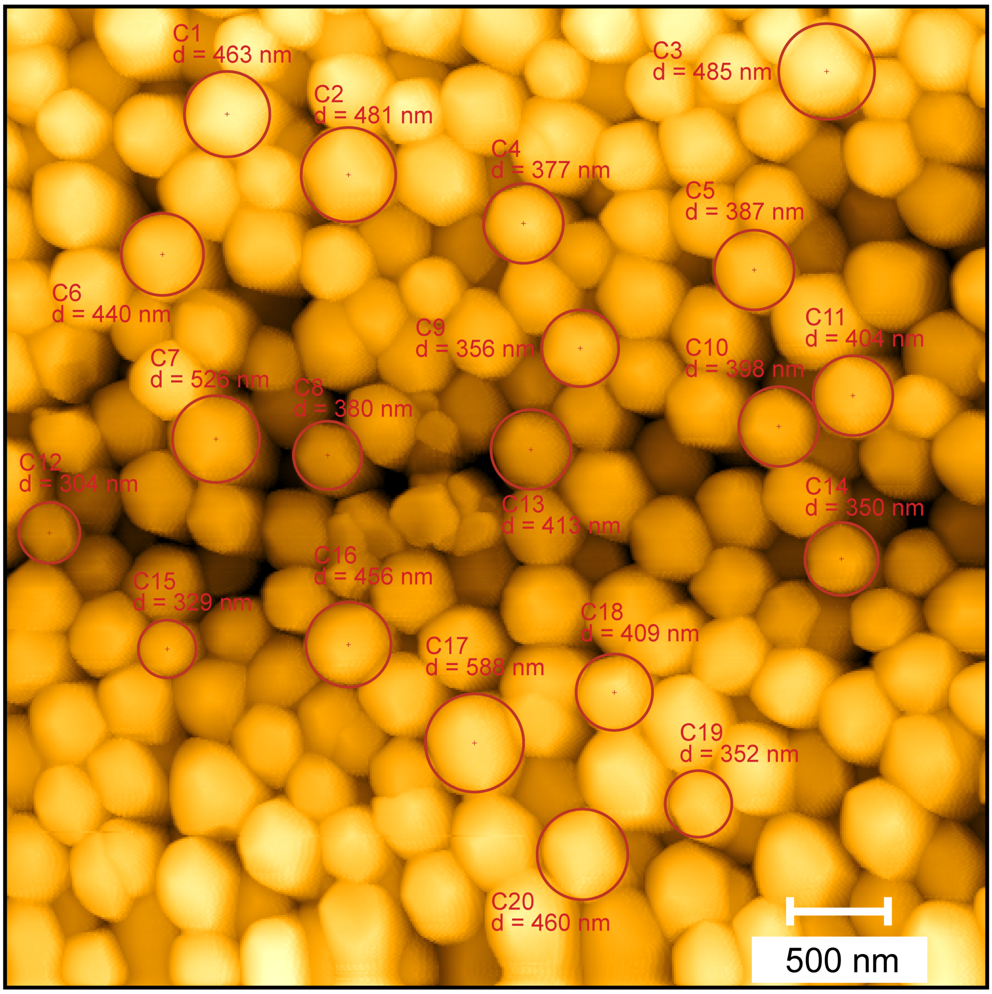

Figure S1. Sampling of individual sub-micron ZIF-8 crystals from an AFM image obtained using a silicon tip (Tap300Al-G) under tapping mode. The averaged nanocrystal size was found to be 417.9 ± 170.1 nm, derived from 20 crystals.

2. Characterization of the geometry of the cube-corner AFM indenter tip

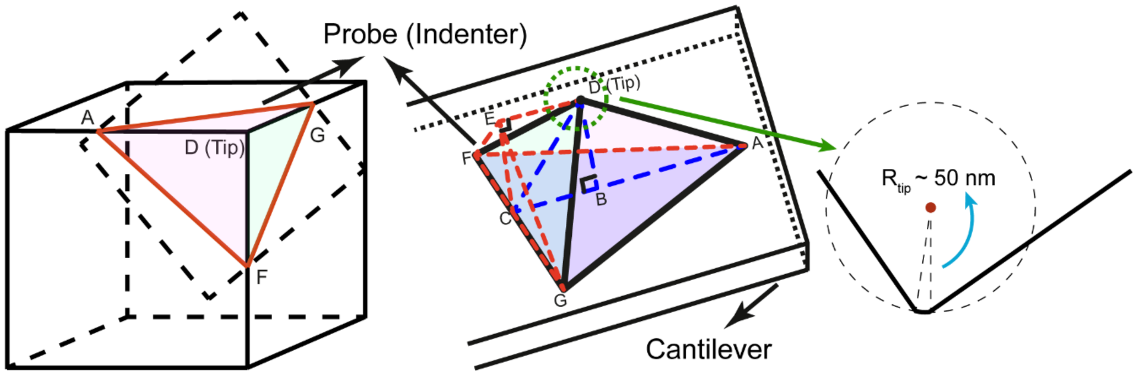

Figure S2. Schematics of the cube-corner indenter used for both AFM imaging and AFM nanoindentation measurements.

According to the manufacturer's specifications of the indenter geometry: Front angle $\angle ADB = 55 \pm 2^{o}$; Back angle $\angle CDB = 35 \pm 2^{o}$; Side angle $\angle CEF = 51 \pm 2^{o}$. At the indentation depth $h_{DB} = 50$ μm, the side length $L_{AB} = 71.4074$ μm; $L_{CB} = 35.0104$ μm; $L_{FC\ (GC)} = 61.7449$ um; $L_{AG\ (AF)} = 123.0332$ um (derived from the Pythagorean Theorem).

The inherent artefacts of AFM imaging are associated with the incomplete convolution between the indenter tip and the sample surface. Typically, certain features of the sample surface, such as protrusions in AFM image become wider than the real ones, likewise holes appear to be narrower and shallower. For the purpose of error reduction, ideally the radius of indenter tip should be smaller than the radius of surface features to be measured. Implementation of a suitable tip deconvolution approach can be used to reduce the imaging errors.[1]

The Villarrubia blind estimation algorithm [2-3] is an indenter reconstruction method, which is able to determine similarly represented indenter geometry based on the fact that AFM image of tested sample contains information of both the sample morphology and tip geometry. In order to extract the tip geometry, the algorithm iterates over at each point of the input AFM image. The algorithm complies with the rationale that when an indenter tip is imaging a surface feature, such as protrusion, in the meantime, the surface protrusion is actually scanning the indenter tip in opposite direction.

As shown in Figure S3(d), usually the features imaged are broadened compared to the actual features of the sample. Conversely, regarding the scanning as a process to image the indenter by surface protrusions as shown in Figure S3(c), these protrusions are actually broadened replicas of the indenter. Therefore, an estimated indenter can be obtained by using a blunt indenter as a reference to fit each point of the three-dimensional image of the sample surface, and subtracting all restricted portion (represented as the regions enclosed by the dashed green boundary and the sample surface boundary, as illustrated in Figure S3(e).

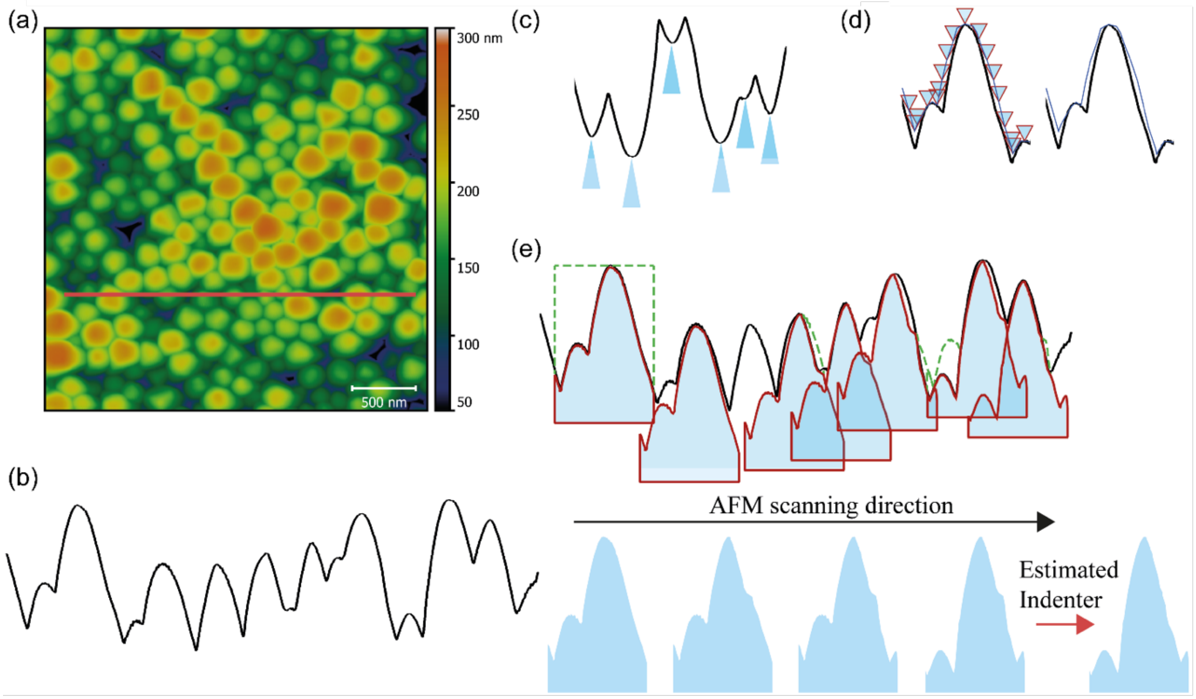

Figure S3. (a) Depth image of polycrystalline ZIF-8 nanocrystals (deposited as a thin-film coating on a glass substrate) obtained by using an AFM PDNISP indenter tip. (b) Profile curve is a one-dimensional topography at the red-line position shown in (a). (c) From a different perspective, AFM tip had been imaged by protrusions of sample surface during the scanning process. (d) AFM images are broadened replicas of the real surface features. (e) Schematic illustration of the procedure of a typical blind indenter tip geometry estimation developed by Villarrubia.[2]

3. Loading scheme of the Veeco Dimension 3100 AFM instrument

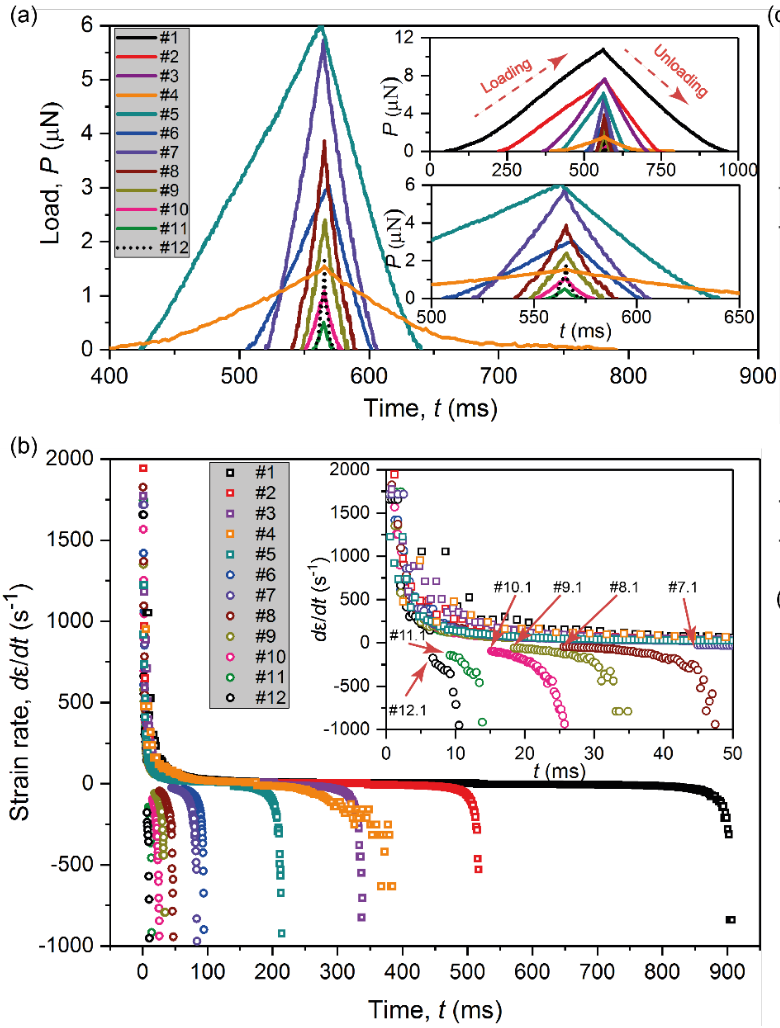

(c)

Numbering	Loading rate *dP/dt* (μN/ms)	Unloading rate *dP/dt* (μN/ms)
#1	0.02510	-0.03000
#2	0.02317	-0.04409
#3	0.04226	-0.05888
#4	0.01134	-0.01506
#5	0.04377	-0.08815
#6	0.05074	-0.09653
#7	0.13045	-0.14747
#8	0.18254	-0.15720
#9	0.13883	-0.13596
#10	0.07475	-0.10079
#11	0.06247	-0.06555
#12	0.24631	-0.21234

(d)

Numbering	Unloading strain rate *dε/dt* (s^{-1})
#7.1	-25.98156
#8.1	-45.79584
#9.1	-59.19862
#10.1	-94.95218
#11.1	-144.62021
#12.1	-178.45653

Figure S4. Loading vs time plot to illustrate the loading scheme of the AFM instrument

As shown in Figure S4, the strain rate decreases continuously with indentation depth during the loading stage. Then after the singularity, i.e. the deepest point ($h_{\max}$), the strain rate increases at the opposite direction until the detachment between the indenter and the specimen occurs. This phenomenon explains why the occurrence of the negative-gradient curve only exists at the incipient segments of the unloading curves. In other words, the increasing unloading strain rate over time is favorable to minimize the effects of creep deformation during the unloading test segment.

The indentation strain rate (s^{-1}) can be correlated to the vertical displacement of the indenter tip, penetrating into the surface:

$$\frac{d\varepsilon}{dt} = \dot{\varepsilon} = \frac{\dot{h}}{h} \tag{S1}$$

In Veeco Dimension 3100 AFM instrument, the load variation over indentation time, $\dot{P} = \partial P/\partial t$, can be maintained constant during each of the indentation cycle (Figure S4). In our experiments, the magnitude of $\dot{P}$ during the loading and unloading test segments can be tuned by varying the AFM scan rate (V) and the cantilever probe deflection (δ). The strain rate at the maximum indentation depth can be determined from $\dot{\varepsilon} = \dot{P}/P_{\max}$,[4] coinciding with the initial point when the indenter starts to unload.

Therefore, in this work, the loading rate ($\dot{P}$) is a controllable parameter. Assuming that hardness (H) of ZIF-8 crystals is homogeneous, i.e. invariant during the entire indentation process, the mathematical expression of the strain rate can be simplified into:

$$\begin{aligned}\dot{\varepsilon} &= c_1\left(\frac{\dot{h}}{h}\right) = c_1\left(\frac{1}{h}\cdot\frac{dh}{dt}\right) = c_1\left(\frac{\sqrt{c_2H}}{\sqrt{P}}\cdot\frac{1}{\sqrt{c_2H}}\cdot\frac{1}{2}\cdot\frac{1}{\sqrt{P}}\cdot\frac{dP}{dt}\right)\\ &= c_1\left(\frac{1}{2P}\cdot\frac{dP}{dt}\right) = \frac{c_1}{2}\cdot\frac{\dot{P}}{P} = c_3\cdot\frac{\dot{P}}{P}\end{aligned} \tag{S2}$$

In Eq.(S2), P is the indentation load that can be expressed in terms of the contact area (A) and hardness (H) as:

$$P = A\cdot H = \frac{\pi h^2 tan\theta}{cos\theta}\cdot H = c_2h^2H \tag{S3}$$

Thus, the indentation depth that can be substituted into Eq.(S2) is:

$$h = \frac{\sqrt{P}}{\sqrt{c_2H}} \tag{S4}$$

where θ in Eq.(S3) is the equivalent conical half-angle, and c_1 to c_3 are material constants that are sample type dependent.

4. AFM nanoindentation of sub-micron sized crystals of ZIF-8 (nanocrystals)

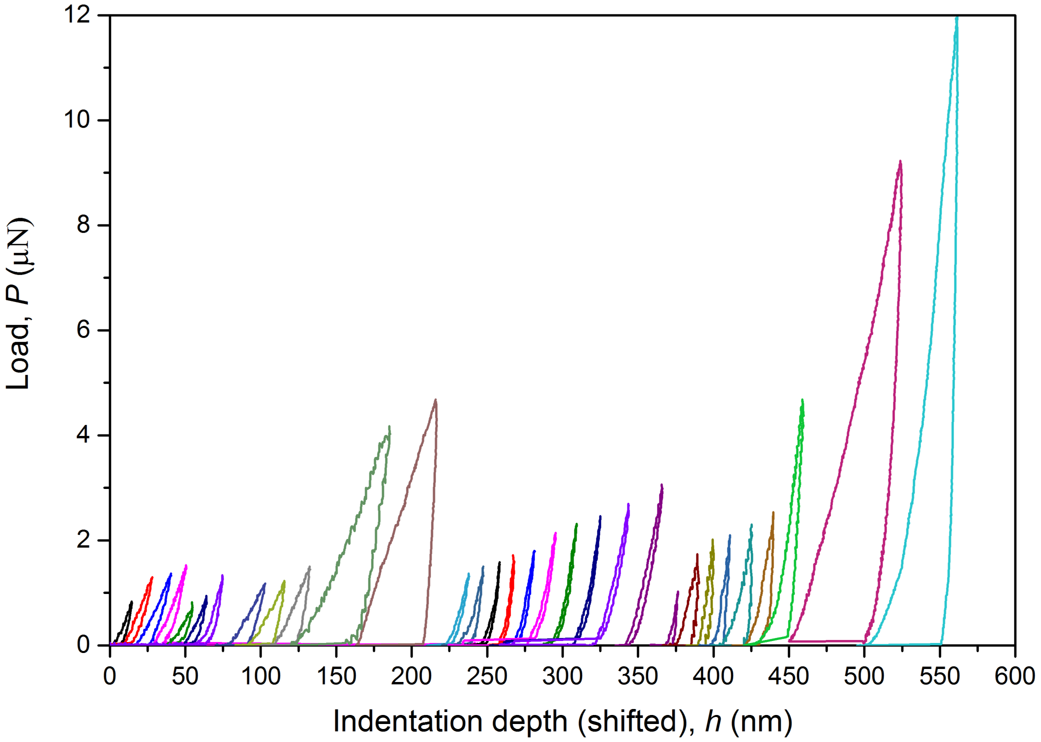

Figure S5. AFM nanoindentation measurements performed on different regions of the (sub-micron) ZIF-8 nanocrystals, deposited as a thin-film coating on a glass substrate (Figure S1).

Localized indentation on polycrystalline specimen is complicated because of the interaction between neighboring crystals. In the perspective of energy storage and dissipation, the work done by indenter might be consumed by either the plastic deformation of crystals or the slippage between crystals. Due to this complexity, the force-displacement curves obtained from the indentation on the polycrystalline coatings show a wide range of curves, some examples are shown in Figure S5.

5. Creep deformation at the point of indenter unloading

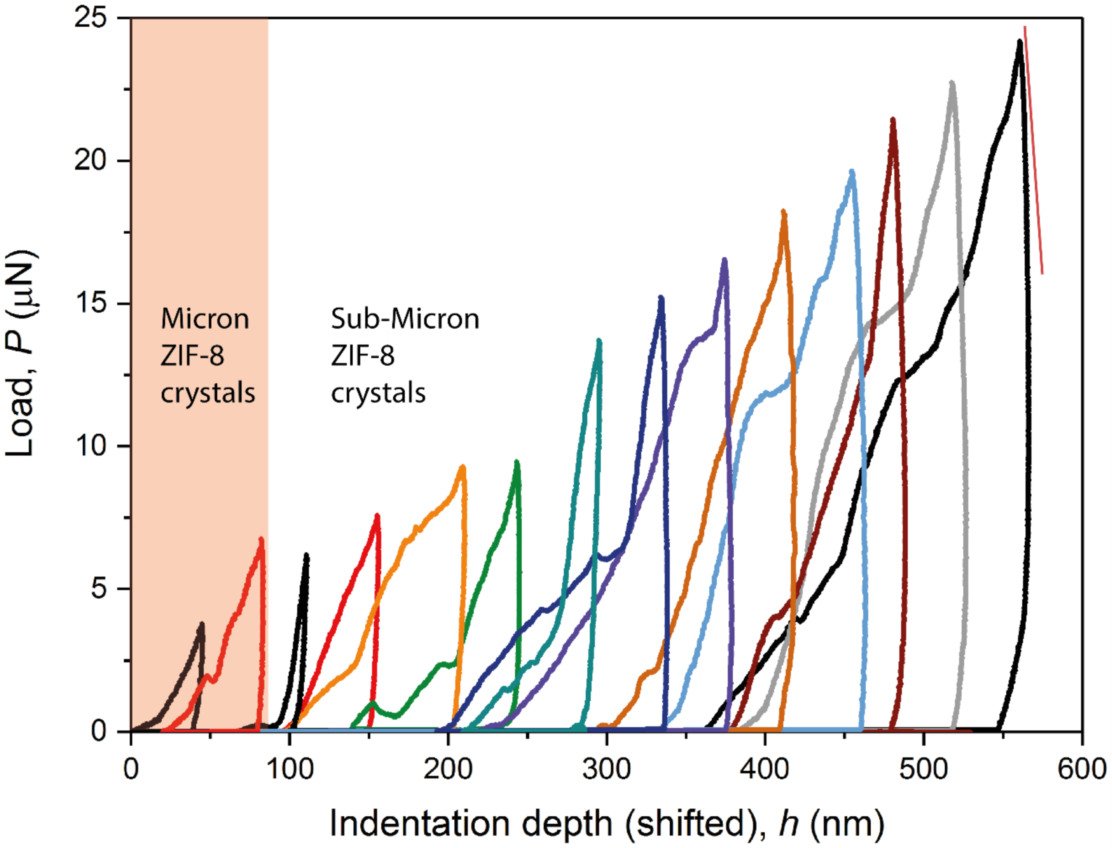

Figure S6. Force-displacement (*P*-*h*) curves for nanoindentation obtained using a high cantilever deflection. Incipient segments of the unloading curves show a negative gradient, $-dP/dh$.

Apparent strain-rate sensitivity effect was observed in ZIF-8 thin film coatings when the unloading strain rate is less than ~60 s^{-1} (Figure 5a). We reasoned that this strain-rate effect is relevant to the negative gradient at the incipient unloading curve as shown in Figure S6. More specifically, indentation with smaller unloading strain rate than a certain threshold value (this is likely to be material dependent, for instance, 60 s^{-1} for ZIF-8), the gradient of the incipient segment of the unloading curve starts to increase, which corresponds to increasing contact stiffness measured until the negative gradient occurs and invalidates the O&P model.[5] Here we found that bulging of the unloading curves of ZIF-8 thin film coatings occurs under imposed high loading conditions, i.e. excessive cantilever deflection.

Since the Oliver and Pharr method[5] has been adopted here, the power law equation cannot fit the negative-gradient segment of the unloading curve. Briscoe *et al.*[4] pointed out that at the incipient segment of the unloading stage, the indentation depth continuously increase slightly with the decreasing forces due to the creep effect. This means that the creep rate surpasses the unloading rate even at the peak force where the highest unloading rate is reached. Cohen *et al.* [6] suggested that this bulging appears due to the fact that a time lag between the change in stress and the induced strain of testing material. In other words, the material has residual "memory" of increasing stress during the incipient stage of unloading. Typical method to eliminate the undesired effect is to hold the maximum indentation load until a mechanical equilibrium is reached (typically adopted in the test procedures of instrumented nanoindenters). This creep effect is apparent in viscoelastic materials such as polymers.

Post-processing, computational approaches can be used to remove this effect by correcting for the contact mechanisms.[4, 7] Negative-gradient unloading curve was also reported on hard materials, such as ceramics, because of grain dislocation. Korobko *et al.*[8] studied the role of point defect in the mechanical properties during nanoindentation. Materials showing viscoplasticity could also be susceptible to this effect leading to a bulging curve in the incipient unloading test segment. Moreover, strong creeping plastic flow of some viscoelastic polymers could be observed.[9] However, another undesired effect, thermal drift, could accompany the creep effect, and this is indistinguishable from the creep contribution.

6. AFM nanoindentation on micron-sized ZIF-8 crystals

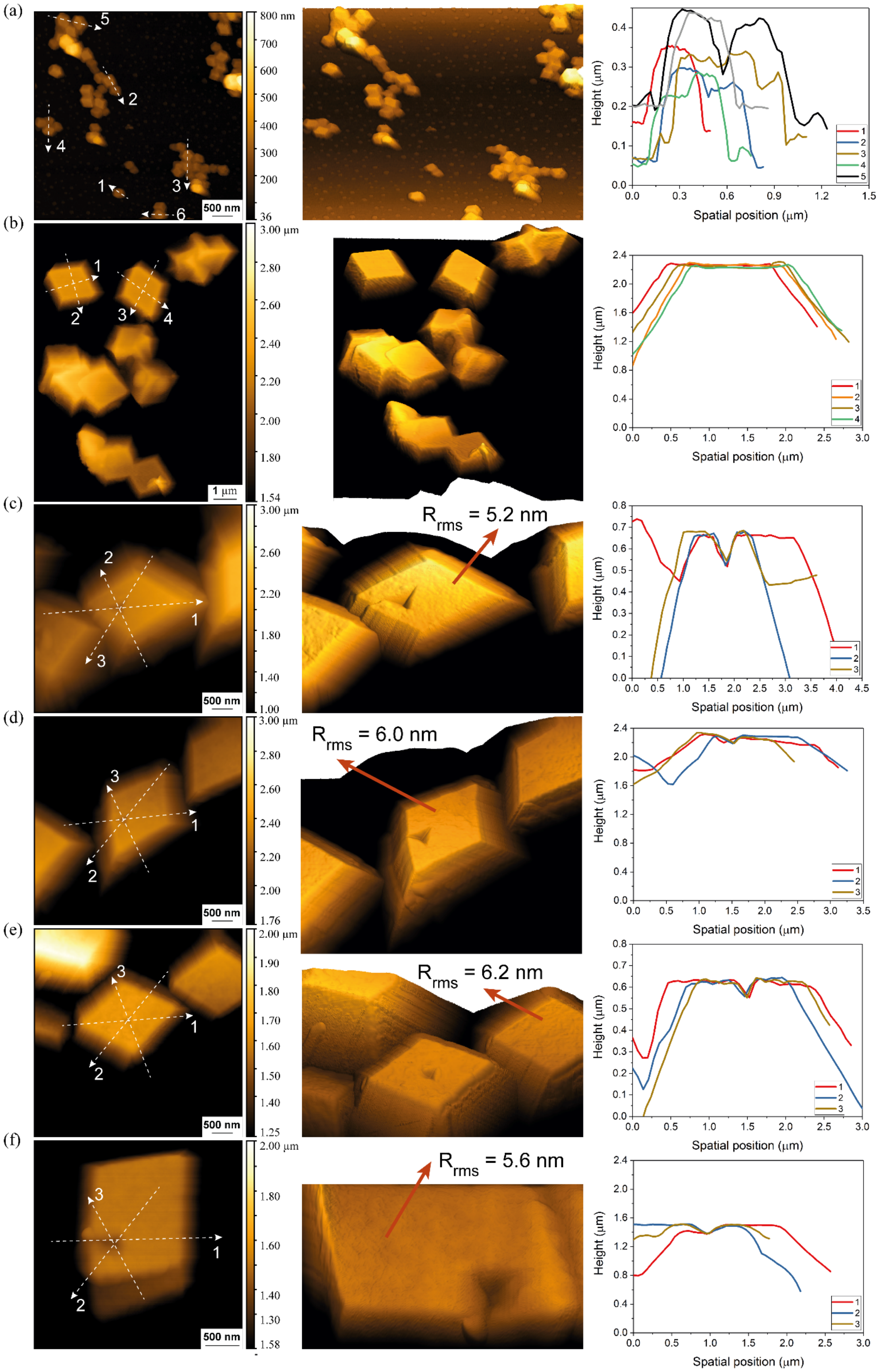

Figure S7. AFM images of indents on individual ZIF-8 crystals: 2D images (left), 3D images (middle); root-mean-square roughness (R_{rms}) of the sample surface. Profile plots (right) derived from the dotted lines marked 1, 2, 3 shown in the left panels.

The micron-sized ZIF-8 crystals studied in this work were approximately 3 μm in height, and thus the measurement of mechanical properties, especially Young's modulus is not affected by the substrate (indentation depth < 10% sample thickness).

The position of the indentation is very important to accurately quantify the mechanical properties measurement. As shown in Figure S7 (c-f), indentations made near to the edges of crystals had resulted into crystal fracture. Mechanical properties such as Young's modulus and hardness derived using such *P-h* curves will be erroneous. Transverse AFM profiles of the four residual impressions in Figure S7 (c-f) can be used to characterize the degree of pile-up and/or sink-in, which will result in deviation of the contact area calculated.

7. Contact adhesion forces at the nanoscale

Adhesion usually has significant influence on the unloading process of the AFM indenter, which exerts and senses nN-μN forces. Under the combined effect of elastic force and adhesive force, the *P-h* curve representing the true response of sample is actually distorted from the pure elastic-plastic deformation. The true interaction force between indenter and sample is given by [10]:

$$P = P_{\mathrm{elastic}} + P_{\mathrm{adhesive}} \tag{S5}$$

The cube-corner indenter contact geometry is converted into equivalent conical indenter geometry based on the same contact area criterion.

$$R_{\mathrm{contact}} = f(h_{\mathrm{contact}}) \tag{S6}$$

Indentation depth of the contact surface is a function of indentation depth from the sample surface [10]:

$$h_{\mathrm{contact}} = (1 - \epsilon_2)h \tag{S7}$$

where $\epsilon_2 = 1 - \frac{2}{\pi}$ for a conical indenter-to-sample contact mechanism. According to the Sneddon solution [11] of elastic behavior for conical indenter, elastic force on sample can be represented by a function of indentation depth.

$$P_{\mathrm{elastic}} = \left(\frac{2E^*}{\pi}\right) tan\,\theta \cdot h^2 \tag{S8}$$

The correlation of actual indenter-sample contact area and indentation depth of an equivalent conical indenter of semi-vertical angle θ is:

$$A_{\mathrm{contact}} = \frac{\pi \cdot tan\,\theta}{cos\,\theta} \cdot {h_{\mathrm{contact}}}^2 \tag{S9}$$

In order to investigate the influence of adhesive force on the sample behavior under indentation process, the energy of adhesion is considered as follows.[10]

$$W_{\mathrm{adhesion}} = -\gamma_{\mathrm{adhesion}} A_{\mathrm{contact}} \tag{S10}$$

where $\gamma_{\mathrm{adhesion}}$ is the thermodynamic work of adhesion.

Substituting Eq.(S4), Eq.(S6) and $\epsilon_2 = 1 - \frac{2}{\pi}$ into Eq.(S7), we obtain an expression for the energy of adhesion. By differentiating energy with respect to the indentation depth, we can obtain the adhesion force, which is:

$$P_{\mathrm{adhesion}} = -\gamma_{\mathrm{adhesion}} \cdot \frac{8 tan\,\theta}{\pi cos\,\theta} \cdot h \tag{S11}$$

Therefore, substituting Eq.(S5) and (S8) into Eq.(S2) gives the *actual* interaction force developed between the indenter and the sample:

$$P = \frac{2E \cdot tan\,\theta}{(1-v^2)\pi} \cdot h^2 - \gamma_{\text{adhesion}} \cdot \frac{8tan\,\theta}{\pi cos\theta} \cdot h \tag{S12}$$

In this work, we propose that the thermodynamic work of adhesion, γ_{adhesion}, can be expressed as a linear function of indentation depth, *h*, which gives:

$$\begin{aligned} P &= \frac{2E \cdot tan\,\theta}{(1-v^2)\pi} \cdot h^2 - (k_1 h + k_2) \cdot \frac{8tan\,\theta}{\pi cos\theta} \cdot h \\ &= \left[\frac{2E \cdot tan\,\theta}{(1-v^2)\pi} - \frac{8k_1 tan\,\theta}{\pi cos\theta}\right] \cdot h^2 - \frac{8k_2 tan\,\theta}{\pi cos\theta} \cdot h \end{aligned} \tag{S13}$$

Table S1. Young's moduli measured by using the O&P method to process load-displacement data obtained from AFM nanoindentation of micron-sized ZIF-8 crystals. Note that the numbering of indents corresponds to the ones in Figure 7 of the main manuscript.

Indentation number #	Young's Modulus E (GPa)	E with adhesion correction (GPa)	$\frac{W_{\mathrm{elastic}}}{W_{\mathrm{plastic}}}$
1	5.365		0.753
2	4.279		0.847
3	5.339	2.385	2.638
4	2.455		0.979
5	4.594		1.370
6	4.343		1.260
7	4.427		0.807
8	4.425		2.120
9	4.807	4.050	1.064
10	5.013	4.485	1.254
11	6.264	3.903	0.857
12	5.140		0.734
13	3.347		0.168
14	1.971		0.607
15	5.088		0.378
16	3.197	2.698	1.828

8. Fracture studies using AFM nanoindentation

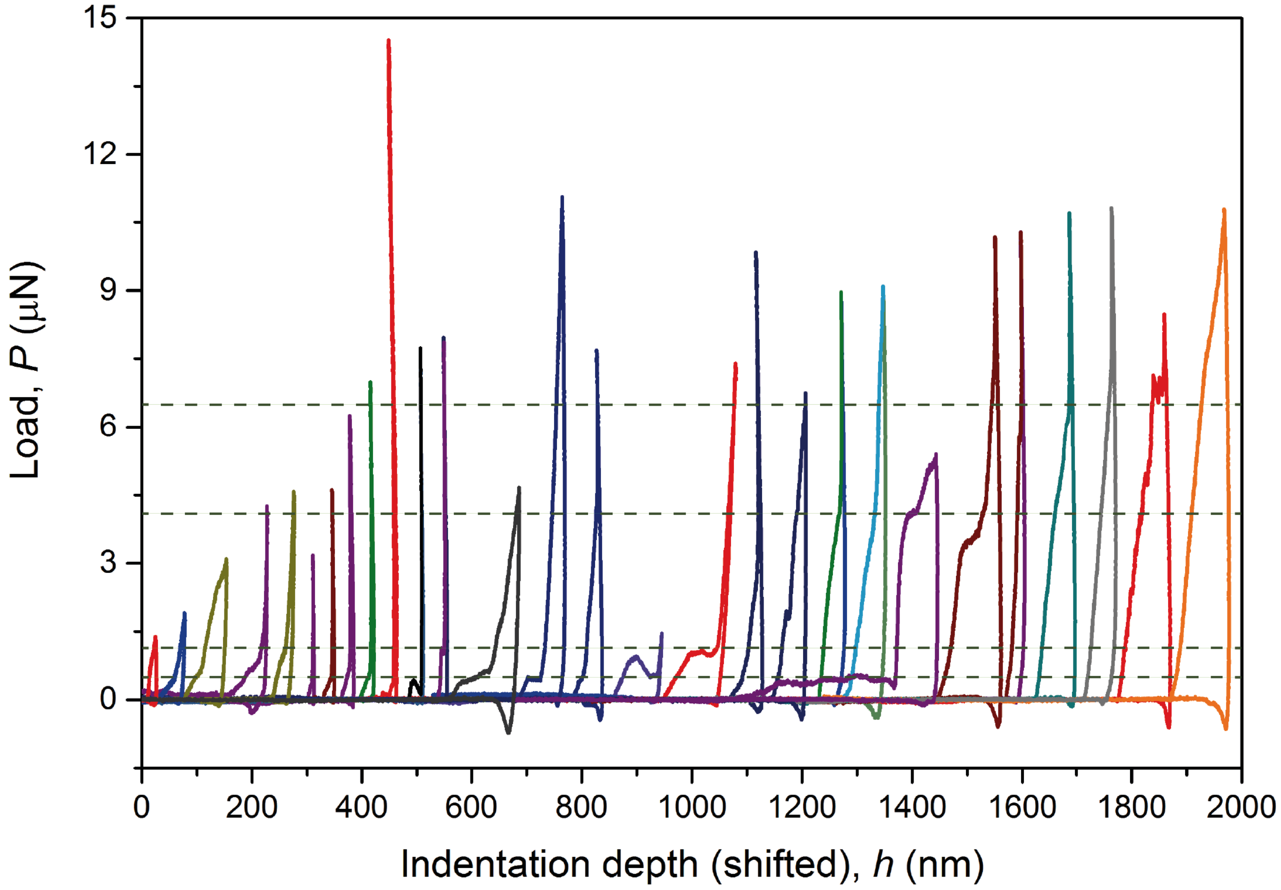

Figure S8. Examples of abnormal *P*-*h* curves obtained from indentation on individual micron-sized ZIF-8 crystals, indicating different failure events; see proposed modes in Figure 12 of the main manuscript.

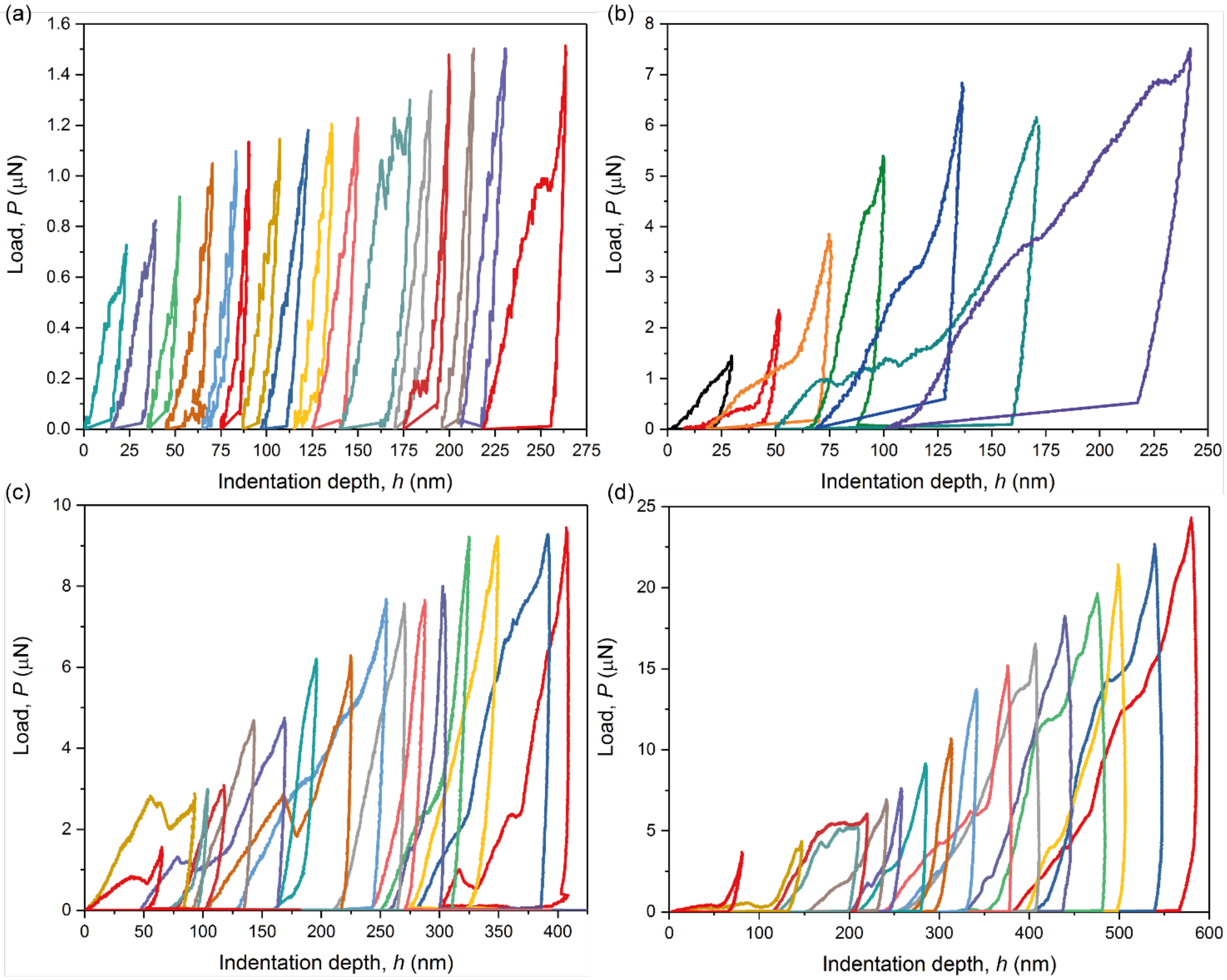

Figure S9. Examples of abnormal *P*-*h* curves (a-d) on polycrystalline ZIF-8 nanocrystals, indicating different failure events; see proposed modes in Figure 11 of the main manuscript.

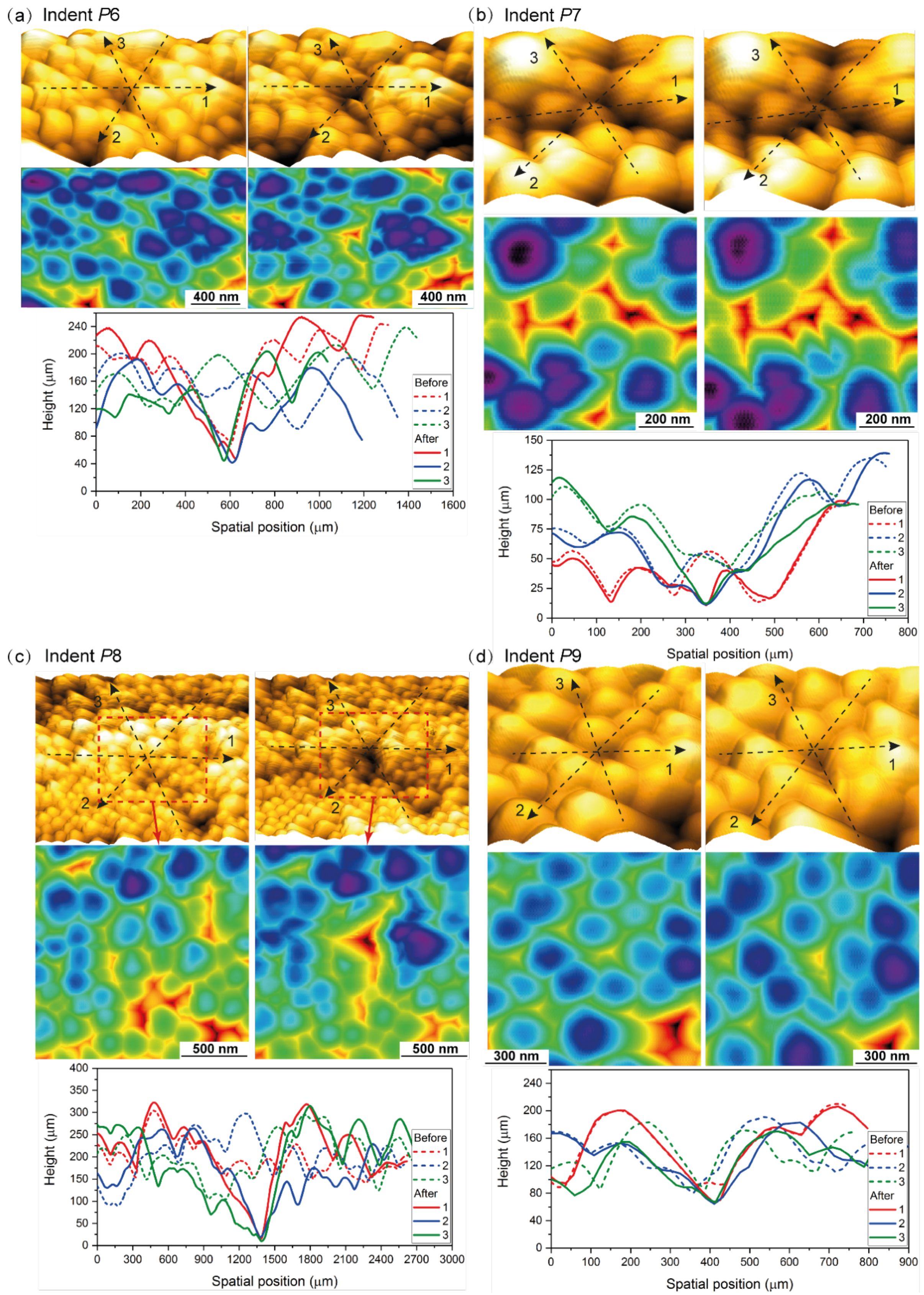

Figure S10. AFM nanoindentation (four examples) on the sub-micron ZIF-8 polycrystalline coatings: (a) Fracture-dominant. (b) Indentation on the interface between two neighboring ZIF-8 crystals. (c) Fracture and interfacial slippage. (d) Cleavage of a ZIF-8 crystal.

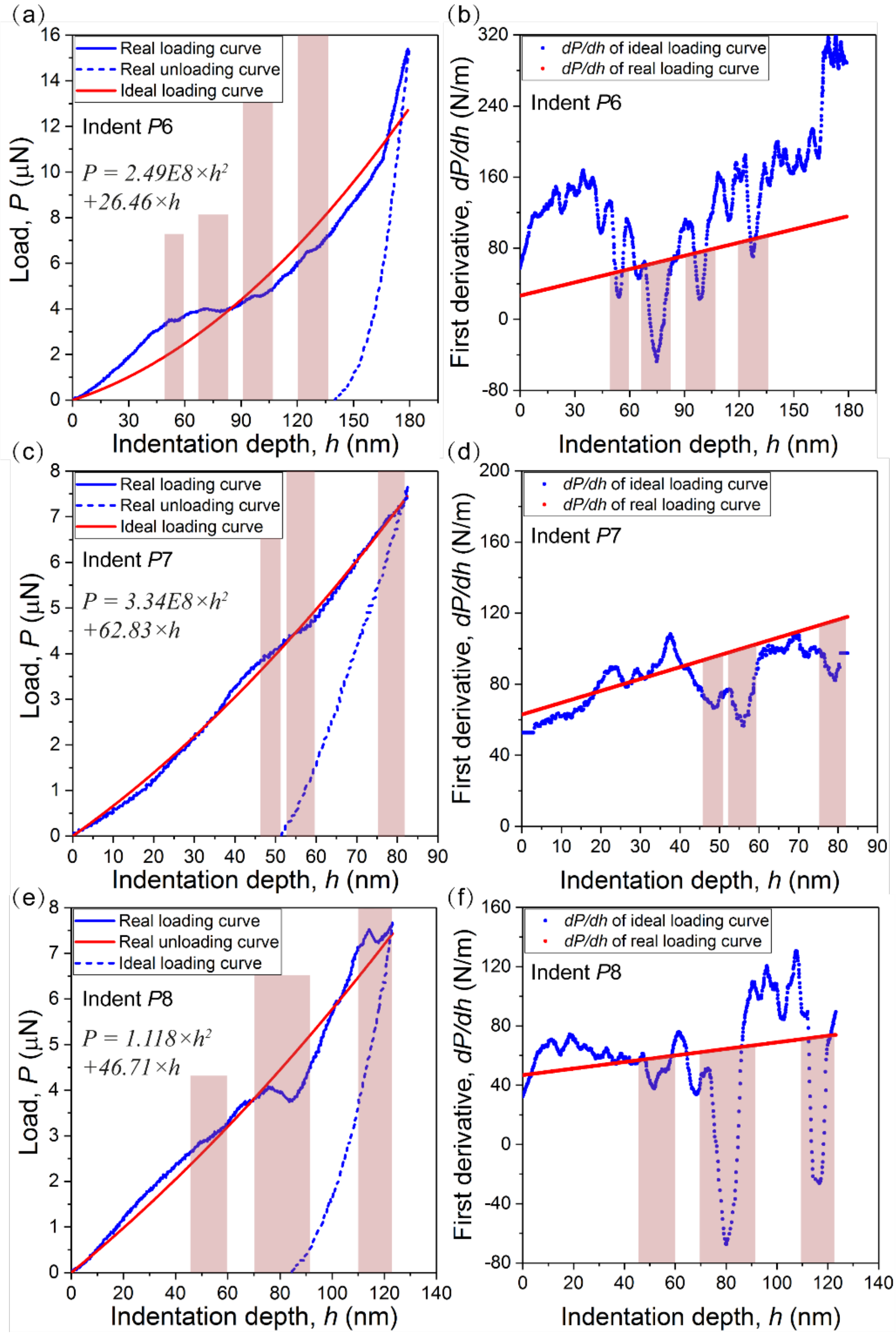

Figure S11. (a, c, e) Force-displacement curves comparing the measured data to the idealized *P-h* curve in accordance with the relation $P(h) = \mathrm{A}h^2 + \mathrm{B}h$, where A and B are curve fitting coefficients. The indent numbers P# correspond to the ones denoted in Figure S10. (b, d, f) Pop-in/sink-in phenomenon where the major events are highlighted, identified by tracking the sharp decline in the contact stiffness, *dP/dh*.

9. Oliver and Pharr (O&P) Method

Four quantities can be extracted from each of the *P-h* curve, they are: (i) the maximum indentation depth, $h_{\max}$; (ii) the maximum load, $P_{\max}$, developed at $h_{\max}$; (iii) the final (permanent) indentation depth after complete unloading, h_{final}; (iv) the elastic contact stiffness, $S = dP/dh$, corresponding to the slope of the incipient segment of the unloading curve of positive gradient. To determine S, we differentiated the segment of the unloading curve fitted with a power-law relation[5]:

$$P(h) = a(h - h_{\text{final}})^b \tag{S14}$$

where a and b are the curve fitting constants.

In the standard O&P model,[5] indentation of the elastic half-space by a rigid axisymmetric indenter is used to model the contact periphery sink-in of an elastic material, but neglecting the pile-up effects caused by elastic-plastic deformation. Therefore, the indentation depth corresponding to the contacting surface is given by:

$$h_{\text{contact}} = h_{\max} - h_{\text{sink-in}} = h_{\max} - \epsilon_1 \frac{P_{\max}}{\left(\frac{dP}{dh}\right)} \tag{S15}$$

where ϵ_1 is a geometrical constant, equivalent to 0.75 for an effective indenter shape that is resembling a paraboloid of revolution.[11] It follows that the real contact area is:

$$A_{\text{contact}} = f(h_{\text{contact}}) \tag{S16}$$

where $f(h_{\text{contact}})$ is the tip area function for a specific indenter geometry. Modern AFM instruments are equipped with accurate depth-sensing and first-surface-contact recognition capabilities, to facilitate the determination of $f(h_{\text{contact}})$ provided that the tip geometry is known. In our analysis, we applied the criterion for first-surface-contact point to be established when the contact stiffness, $S \geq 25$ N/m. The value of A_{contact} can then be found and applied for calculating the "indentation hardness", defined by:

$$H = \frac{P_{\max}}{A_{\text{contact}}} \tag{S17}$$

Likewise, accurate determination of the magnitude of A_{contact} is important for quantification of the effective (reduced) modulus, in accordance with O&P[5]:

$$E_{\text{effective}} = \frac{1}{2\beta} S \frac{\sqrt{\pi}}{\sqrt{A_{\text{contact}}}} \tag{S18}$$

where β is a dimensionless correction factor to account for non-symmetrical pyramidal shape of the indenter tip. Using finite-element analysis and analytical method, Hay *et al.*[12] developed the following expression to approximate the β parameter for an equivalent conical indenter:

$$\beta = \frac{\pi[\frac{\pi}{4} + 0.1548\, cot\, \theta\, \frac{1-2v}{4(1-v)}]}{[\frac{\pi}{2} - 0.8312\, cot\, \theta\, \frac{1-2v}{4(1-v)}]^2} \tag{S19}$$

where θ is the included half-angle of the indenter. Because the axisymmetric equivalence of the cube-corner indenter is a cone, for the indenter tip used in this work the value of θ was 45.7333°. In this study, the Poisson's ratio (v) of ZIF-8 was taken as 0.4, corresponding to that of a polycrystalline (isotropic aggregate of) ZIF-8.[13] Applying Eq.(S16), we obtained $\beta = 1.1093$.

Because the stiffness of the diamond indenter tip (1141 GPa) is substantially higher than that of the MOF sample to be probed (typically in the range of several GPa [14]), we may simplify

$$\frac{1}{E_{\mathrm{effective}}}=\frac{1-{v_{\mathrm{sample}}}^2}{E_{\mathrm{sample}}}+\frac{1-{v_{\mathrm{indenter}}}^2}{E_{\mathrm{indenter}}}\approx\frac{1-{v_{\mathrm{sample}}}^2}{E_{\mathrm{sample}}} \tag{S20}$$

The elastic modulus of the tested sample can be expressed as:

$$E_{\mathrm{sample}}=\frac{1}{2\beta}(1-v^2)S\frac{\sqrt{\pi}}{\sqrt{A_{\mathrm{contact}}}} \tag{S21}$$

10. Key factors that could introduce errors in the AFM nanoindentation measurements

Surface detection errors:

If the contact point between indenter and specimen was misidentified, mechanical properties determined will be affected, especially for shallow indentation and soft materials. These errors are due to erroneous indentation depth and contact area. For instance, misidentification of contact point in indentation on PuraMatrix-collagen hydrogels could bring about almost 5 times overestimation of indentation modulus.[15] Several approaches have been developed in order to reduce the surface detection errors, see refs.[16-17]

Sample roughness:

Specimen surface roughness and asperities could distort the *P-h* curve and will affect the accuracy of tip contact area determination.

Erroneous spring constant of AFM cantilever probe:

Accurate measurement of spring constant of the AFM cantilever, on which the indenter is mounted, is a pivotal factor in order to obtain accurate *P-h* curves. There are many techniques proposed for obtaining spring constants of AFM cantilevers, but each with certain limitations. Typical techniques describing their uncertainties, advantages, and disadvantages can be found in ref.[18]

Non-ideal indenter geometry:

Real indenters usually deviate from the ideally presumptive geometry, and this deviation results in erroneous contact area and invalidates the application of idealized contact theories. The influence of non-ideal indenter geometry is more pronounced for shallow indentation, such as AFM nanoindentation. Moreover, pile-up and sink-in are two phenomena, which are closely associated with the geometry of the indenter used. Therefore, efforts have been done to quantify the effect of geometric deviation on mechanical property measurement *via* both analytical[19] and experiment[20] methods.

Deformation of the indenter in hardness test:

In the majority of contact theories, a rigid indenter is assumed to simplify the analysis of indentation data. Nevertheless, with regards to indentation on stiff and hard materials, the contact area is usually underestimated. In order to correct for this deviation, further development of improved contact theories has been made. For instance, modulus and hardness of a specimen measured by a new method developed on the basis of the Hertz contact theory are closer to the actual magnitudes than those derived from the Sneddon's solution.[21]

References

1. Markiewicz, P.; Goh, M. C. Atomic Force Microscope Tip Deconvolution Using Calibration Arrays. *Rev. Sci. Instrum.* **1995,** *66*, 3186-3190.

2. Villarrubia, J. S. Algorithms for Scanned Probe Microscope Image Simulation, Surface Reconstruction, and Tip Estimation. *J. Res. Natl. Inst. Stand. Technol.* **1997,** *102*, 425-454.

3. Dongmo, L. S.; Villarrubia, J. S.; Jones, S. N.; Renegar, T. B.; Postek, M.; Song, J. F. Experimental Test of Blind Tip Reconstruction for Scanning Probe Microscopy. *Ultramicroscopy* **2000,** *85*, 141-153.

4. Briscoe, B. J.; Fiori, L.; Pelillo, E. Nano-Indentation of Polymeric Surfaces. *J. Phys. D-Appl. Phys.* **1998,** *31*, 2395-2405.

5. Oliver, W. C.; Pharr, G. M. Measurement of Hardness and Elastic Modulus by Instrumented Indentation: Advances in Understanding and Refinements to Methodology. *J. Mater. Res.* **2004,** *19*, 3-20.

6. Cohen, S. R.; Kalfon-Cohen, E. Dynamic Nanoindentation by Instrumented Nanoindentation and Force Microscopy: A Comparative Review. *Beilstein J. Nanotechnol.* **2013,** *4*, 815-833.

7. Feng, G.; Ngan, A. H. W. Effects of Creep and Thermal Drift on Modulus Measurement Using Depth-Sensing Indentation. *J. Mater. Res.* **2002,** *17*, 660-668.

8. Korobko, R.; Kim, S. K.; Kim, S.; Cohen, S. R.; Wachtel, E.; Lubomirsky, I. The Role of Point Defects in the Mechanical Behavior of Doped Ceria Probed by Nanoindentation. *Adv. Funct. Mater.* **2013,** *23*, 6076-6081.

9. Moeller, G. AFM Nanoindentation of Viscoelastic Materials with Large End-Radius Probes. *J. Polym. Sci., Part B: Polym. Phys.* **2009,** *47*, 1573-1587.

10. Sirghi, L.; Rossi, F. Adhesion and Elasticity in Nanoscale Indentation. *Appl. Phys. Lett.* **2006,** *89*, 243118.

11. Sneddon, I. N. The Relation between Load and Penetration in the Axisymmetric Boussinesq Problem for a Punch of Arbitrary Profile. *Int. J. Eng. Sci.* **1965,** *3*, 47-57.

12. Hay, J. C.; Bolshakov, A.; Pharr, G. M. A Critical Examination of the Fundamental Relations Used in the Analysis of Nanoindentation Data. *J. Mater. Res.* **1999,** *14*, 2296-2305.

13. Tan, J. C.; Civalleri, B.; Lin, C. C.; Valenzano, L.; Galvelis, R.; Chen, P. F.; Bennett, T. D.; Mellot-Draznieks, C.; Zicovich-Wilson, C. M.; Cheetham, A. K. Exceptionally Low Shear Modulus in a Prototypical Imidazole-Based Metal-Organic Framework. *Phys. Rev. Lett.* **2012,** *108*, 095502.

14. Tan, J. C.; Cheetham, A. K. Mechanical Properties of Hybrid Inorganic-Organic Framework Materials: Establishing Fundamental Structure-Property Relationships. *Chem. Soc. Rev.* **2011,** *40*, 1059-1080.

15. Kaufman, J. D.; Klapperich, C. M. Surface Detection Errors Cause Overestimation of the Modulus in Nanoindentation on Doft Materials. *J. Mech. Behav. Biomed. Mater.* **2009,** *2*, 312-317.

16. Crick, S. L.; Yin, F. C.-P. Assessing Micromechanical Properties of Cells with Atomic Force Microscopy: Importance of the Contact Point. *Biomech. Model. Mechanobiol.* **2007,** *6*, 199-210.

17. Gavara, N. Combined Strategies for Optimal Detection of the Contact Point in AFM Force-Indentation Curves Obtained on Thin Samples and Adherent Cells. *Sci. Rep.* **2016,** *6*.

18. Burnham, N. A.; Chen, X.; Hodges, C. S.; Matei, G. A.; Thoreson, E. J.; Roberts, C. J.; Davies, M. C.; Tendler, S. J. B. Comparison of Calibration Methods for Atomic-Force Microscopy Cantilevers. *Nanotechnology* **2003,** *14*, 1-6.

19. Borodich, F. M.; Keer, L. M.; Korach, C. S. Analytical Study of Fundamental Nanoindentation Test Relations for Indenters of Non-Ideal Shapes. *Nanotechnology* **2003,** *14*, 803-808.

20. McElhaney, K. W.; Vlassak, J. J.; Nix, W. D. Determination of Indenter Tip Geometry and Indentation Contact Area for Depth-Sensing Indentation Experiments. *J. Mater. Res.* **1998,** *13*, 1300-1306.

21. Lo, R. Y.; Bogy, D. B. Compensating for Elastic Deformation of the Indenter in Hardness Tests of Very Hard Materials. *J. Mater. Res.* **1999,** *14*, 2276-2282.